Residual stresses in LENS-deposited AISI 410 stainless steel plates

Liang Wang[a], Sergio D. Felicelli[b,*], Phillip Pratt[b]

[a] *Center for Advanced Vehicular Systems, Mississippi State University, Mississippi State, MS 39762, USA*
[b] *Mechanical Engineering Department, Mississippi State University, Mississippi State, MS 39762, USA*

ARTICLE INFO

ABSTRACT

The residual stress in thin plate components deposited by the laser engineered net shaping (LENS®) process was investigated experimentally and numerically. Neutron diffraction mapping was used to characterize the residual stress in LENS-deposited AISI 410 stainless steel thin wall plates. Using the commercial welding software SYSWELD, a thermo-mechanical three-dimensional finite element model was developed, which considers also the effect of metallurgical phase transformations. The model was employed to predict the temperature history and the residual stress field during the LENS process. Several simulations were performed with the geometry and process parameters that were used to build the experimental samples. The origin of the residual stress distribution is discussed based on the thermal histories of the samples, and the modeling results are compared with measurements obtained by neutron diffraction mapping.

© 2008 Elsevier B.V. All rights reserved.

1. Introduction

Laser engineered net shaping (LENS®) is a rapid manufacturing process for fabricating three-dimensional metal parts with high strength and ductility directly from computer aided design (CAD) solid model [1,2]. LENS components have been fabricated from a variety of materials such as low-alloy steels [3], stainless steel [4,5], nickel-based alloys [6,7], and titanium alloys [8,9]. The LENS process involves rapid heating and cooling rates, and yields thermal, metallurgical, and mechanical phenomena resulting in non-uniform strain and stress fields. The residual stress has a significant effect on corrosion, fracture resistance, and fatigue performance of the LENS components. Therefore, an understanding of the origin of the residual stress will aid in reducing the stress by either the optimization of the process parameters during fabrication or by subsequent heat treatment in order to produce high quality LENS components.

In general, the residual stress induced in the LENS components might be attributed to dislocations produced by high cooling rates, solid–solid phase transformations, or thermal shrinkage [10]. The residual stress in LENS components has been investigated both by experiments [11–14] and modeling [10,15,16]. Rangaswamy et al. [11,12] measured the residual stresses in LENS components using neutron diffraction and contour method. The measurements were performed in the three orthogonal symmetry directions of the part using thin wall and square pillar LENS samples. The results revealed that the stress was uniaxial, with compression at the center of the samples, tension at the edges and aligned along the growth direction. This may occur if the edges are hotter than the interior. In this case, the shrinkage of the outside is constrained by the cooler interior. However, there is no modeling work that explains the effects of the thermal history on the residual stress distribution. Vasinonta et al. [15] developed a two-dimensional thermo-mechanical model to investigate the residual stress in the LENS process. The results indicated that changing laser velocity and power can reduce residual stresses by as much as 20% from the yield stress. However, a two-dimensional model was used to calculate the stress component only in the travel direction and no experimental comparison was provided. Stresses and deformations in other layered manufacturing processes have also been investigated [17]. An experimental/numerical investigation on the effects of the LENS process parameters on the residual stress distribution is not yet available in the literature.

In this paper, a three-dimensional thermo-mechanical finite element model is developed to simulate multilayer LENS deposition of AISI 410 stainless steel (SS410) powder. The development of the model was carried out using the SYSWELD software package [18,19]. The model is used to calculate the thermal cycles, molten pool size, solid phase transformation, and the residual stress in the LENS process. Specifically, the influence of laser travel speed and laser power on the distribution of residual stresses in the fabricated part is studied. The simulated results are then compared with measured data of residual stress by neutron diffraction in thin plates built with the LENS process under different process parameters.

* Corresponding author. Tel.: +1 662 325 1201.
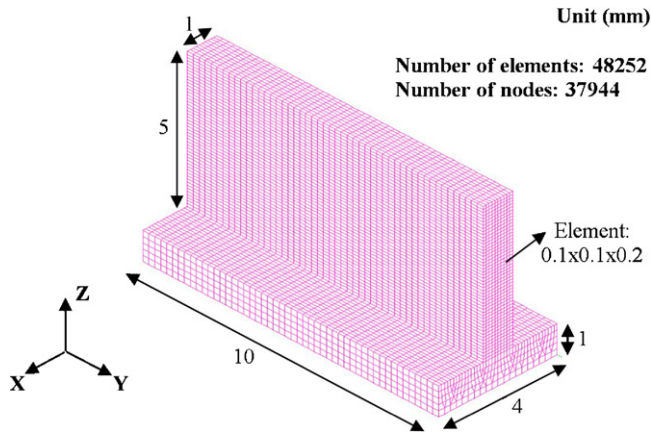*E-mail address:* felicelli@me.msstate.edu (S.D. Felicelli).

Fig. 1. Geometry and mesh of a 10-layer single wall plate used in this study.

Fig. 2. Laser power used in the study. (a) Laser power distribution at each pass for different laser travel velocities. (b) Laser power intensity along the travel direction from one side to another in each pass.

2. Finite element modeling

The geometry and finite element mesh used in the model are shown in Fig. 1. The plate structure was built by overlapping 10 single tracks of material, each with a length of 10.0 mm, a thickness of 0.5 mm and a width of 1.0 mm. The plate was fabricated on the surface of a substrate 1 mm-thick, 4 mm-wide and 10 mm-long. Three values of the laser travel speed were explored: 2.5, 4.2, and 8.5 mm/s. The laser beam moves in the same direction (left to right) for each pass. A dense mesh was used for the plate and the contact area with the substrate, where higher thermal gradients are expected. There are a total of 37,944 nodes and 48,252 elements in the mesh of the computational domain.

An optimized time-stepping scheme was employed to achieve fast convergence of the solution and reasonable accuracy. The substrate and the deposited plate material are both made of SS410. The thermal and mechanical properties used in the model were those provided in the software database for the material X20Cr13 with chemical composition as follows: $0.16\% \leq C \leq 0.25\%$, $12.0\% \leq Cr \leq 14.0\%$, $Mn \leq 1.5\%$, $Si \leq 1.0\%$, $S \leq 0.03\%$, and $P \leq 0.04\%$, which is almost identical to the chemical composition of SS410. Temperature-dependent thermal and mechanical properties were measured and tabulated by extensive experimentation and supplied with the software. It was assumed that the substrate material is initially at room temperature, T_0 (no pre-heating). A fixed temperature boundary condition equal to the room temperature is prescribed on the bottom surface of the substrate. The boundary conditions for all other surfaces take into account both laser heating and heat losses due to surface convection and radiation. Parameters corresponding to a Nd:YAG laser are used in the calculation. The laser beam power is modeled as a Gaussian profile with a conical shape, described by the equation [20]:

$$Q_r = \frac{2P}{\pi r_0^2 H}\left(1 - \frac{z}{H}\right)\exp\left(1 - \left(\frac{r}{r_0}\right)^2\right) \tag{1}$$

where Q_r is the input energy density (W/mm^3), P the absorbed laser beam power (W), r_0 the initial radius of the laser beam (at the top of the keyhole, $r_0 = 0.5$ mm, then the laser beam size increases up to 1.0 mm), H the maximum depth (=0.5 mm), r the current radius, and z is the current depth. The moving heat source was modeled by a user subroutine in SYSWELD. In this study, the heat source was calibrated with the measured dimensions of the molten pool images and the temperatures profiles surrounding the molten pool, which were presented in Ref. [21]. A comprehensive description of the thermo-metallurgical model was presented in Refs. [22–26].
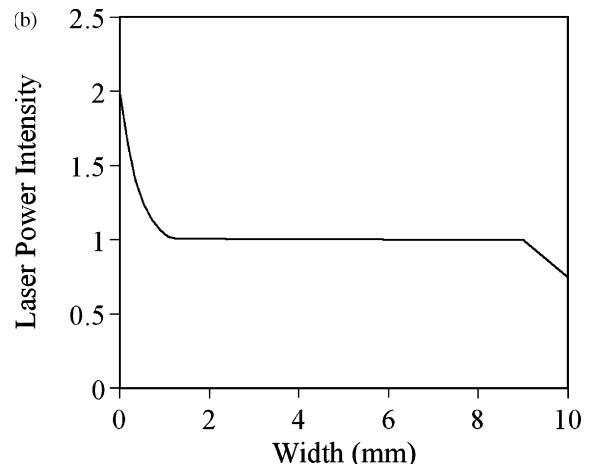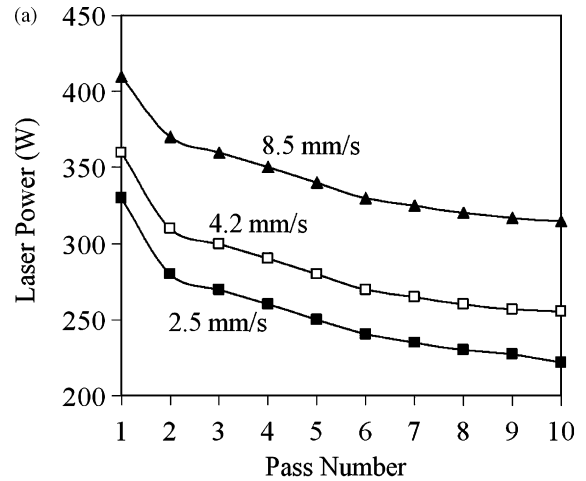
The calculated thermal fields and solid phase transformations were used as input conditions for the mechanical analysis. In SYSWELD [17], the total strain is partitioned as follows:

$$E^t = E^e + E^{thm} + E^{pc} + E^{pt} \tag{2}$$

where E^e is the macroscopic elastic strain, E^{thm} is the macroscopic thermo-metallurgical strain, E^{pc} is the classical macroscopic plastic strain, and E^{pt} is the transformation-induced-plasticity strain. The elastic strain is modeled using the isotropic Hook's law with temperature-dependant Young's modulus and Poission's ratio supplied with the SYSWELD software. The thermo-metallurgical strain is modeled by taking into account the expansion and contraction produced by the metallurgical transformations. The strains due to thermal and metallurgical factors are expressed as

$$E^{thm} = \sum f_i E_i^{thm}(T) \tag{3}$$

where $E_i^{thm}(T)$ is the thermal strain of phase i at temperature T, and f_i is the phase proportion of phase i. For the conventional plastic strain, an isotropic strain-hardening model is employed. The transformation plastic strain is modeled based on the phenomenon called "transformation plasticity". Due to the difference of volume between the various phases, a plastic flow takes place tending to reduce the stresses to zero during the metallurgical transformations in the presence of residual stress. This phenomenon may occur
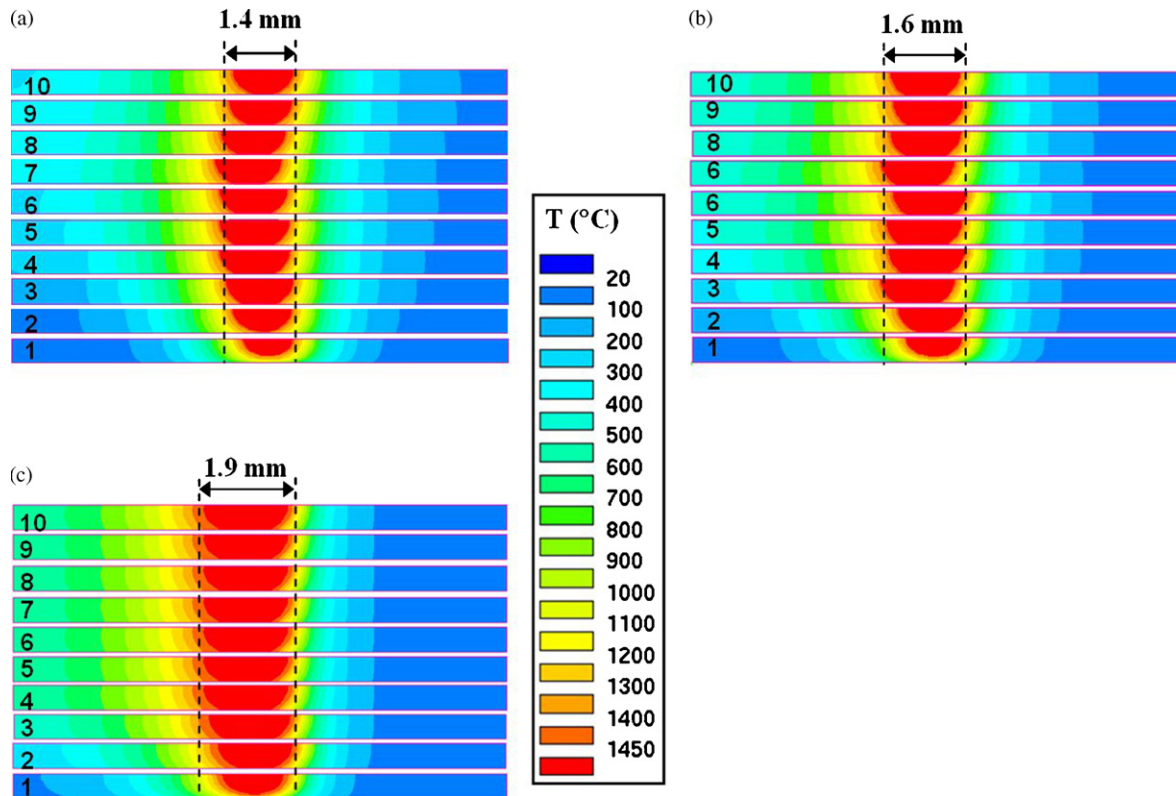
Fig. 3. Molten pool size when the laser beam moves to the center of the plate for each layer at (a) 2.5 mm/s; (b) 4.2 mm/s; (c) 8.5 mm/s.

even in the absence of external stresses. A full explanation of the material constitutive model is given in Ref. [17].

3. Results and discussions

3.1. Residual stresses measurements

Using the method of neutron diffraction, strain measurements were taken at the high flux isotope reactor (HFIR) facility at Oak Ridge National Laboratory (ORNL) for seven LENS-produced thin wall samples of stainless steel AISI 410. The samples were produced at the facilities of Optomec® in Albuquerque, NM. The plates were made by varying three process parameters: laser power, laser travel speed, and metal powder flow rate. The goal of the neutron measurements was to determine how the magnitude and distribution of residual stresses in the plates was affected by varying these input parameters. The experimental setup and results were presented in detail elsewhere [27].

3.2. Thermal analysis

The thermo-metallurgical model was previously calibrated with experiments through the thermal images of the molten pool and surrounding area [21]. The thermal images of a SS410 single wall build were obtained using a two-wavelength imaging pyrometer. The experiments were performed in a LENS 850 machine with a 3 kW IPG laser for different process parameters. Numerical analysis using a three-dimensional finite element method showed a good capability of the model to predict the temperature distribution and molten pool size. A good agreement between the experimental and numerical results was obtained for molten pool size and temperature distribution in the molten pool. In this study, the laser power was adjusted according to the following criteria: (1) to obtain steady

molten pool size; (2) one and a half layers are melted in order to achieve good bonding between layers.

Fig. 2(a) shows the laser power programs used in order to obtain molten pools that satisfy the above criteria for the three-laser travel velocities. Higher laser power is required for higher laser travel speed in order to melt one and a half layers. The laser power also decreases as the part is built up in order to compensate for the smaller effect of the substrate and keep a steady molten pool size. When depositing along a layer, the laser power also needs to be regulated in order to control the pool size. At the beginning of each pass, a higher laser power is required in order to maintain pool size because this region has cooled down during the idle time between layers; similarly, a lower laser power is used at the end of each pass to compensate for the heat built up during the layer pass. This change of laser power along a layer sweep is achieved by affecting the laser power with laser power intensity, as shown in Fig. 2(b). The actual laser power is equal to the product of the nominal laser power (shown in Fig. 2(a)) and the laser power intensity of Fig. 2(b). For the three values of travel speed simulated (2.5, 4.2 and 8.5 mm/s), the average laser powers were 254, 285 and 344 W, respectively.

Fig. 3 shows the molten pool size distribution for each layer at different laser travel velocities. The molten pool size is similar for each layer except the first layer, which is close to the substrate and difficult to be completely melted due to the large heat sink of the substrate. The molten pool size increases with the laser travel velocity. The average molten pool sizes are 1.4, 1.6, and 1.9 mm for the three-laser travel velocities, respectively.

Fig. 4 shows the thermal cycles at the center of the plate for each layer at different laser travel velocities. Due to the high cooling rate produced by the substrate, the temperature of the first 4 or 5 layers cools down to near the room temperature before a new layer is deposited. However, for the upper layers, the effect of the
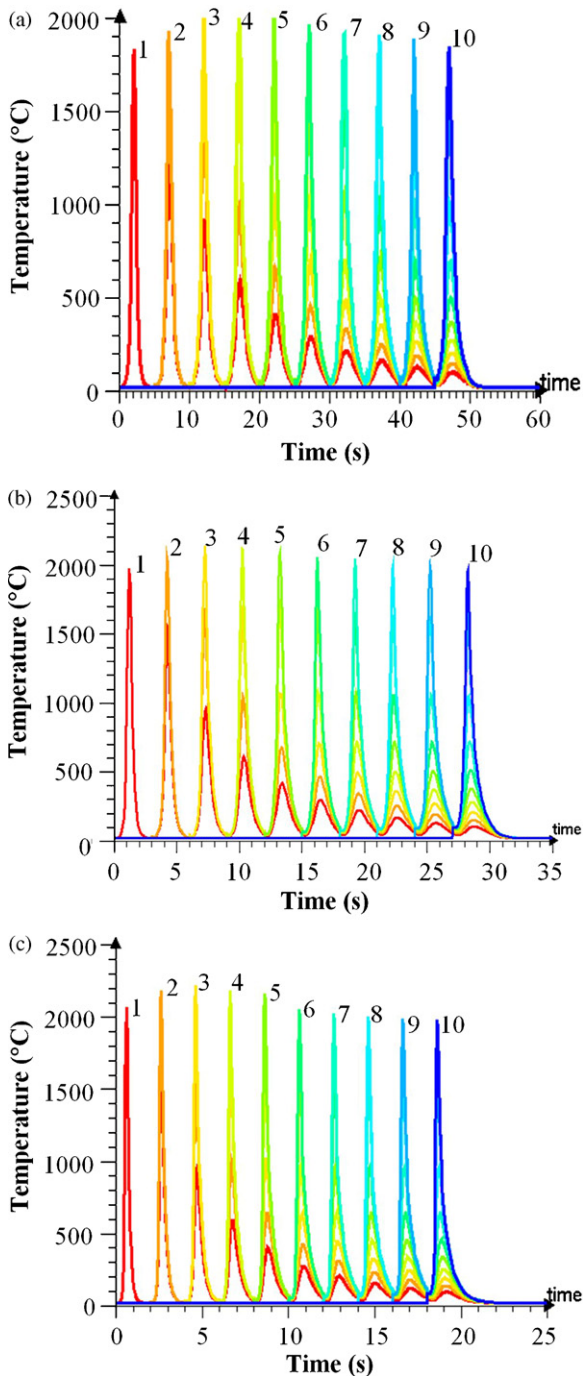
Fig. 4. Thermal cycles at the center of the plate for each layer at (a) 2.5 mm/s; (b) 4.2 mm/s; (c) 8.5 mm/s.

substrate is reduced, and the accumulation of thermal energy at the end of each cycle causes the temperature to be somewhat higher than that at the end of its previous cycle. This is observed, for example, in Fig. 4(b), where the temperature at the center of layer #8 cools down to approximately 100 °C before layer #9 is deposited. An adjustment of the idle time also needs to be done in the model. In the experiments, there is negligible idle time from one layer deposition to another. In order to save computation time, the model height and width are smaller than those of the samples used in the experiments. In particular, the width of the plate is 10 mm in the model and 25 mm in the experiments. Therefore, a longer idle time is used in the model in order to match the cooling time before

starting the deposition of a new layer. This is the same technique used in Ref. [23]. The peak temperature observed in Fig. 4 is around 1850–2200 °C. Note that the peak temperature is basically independent on the laser travel velocity as well as on the laser power. This can be attributed to the control of the laser power in order to melt one and a half layer and keep stable molten pool size for each case. It is also noticed that similar thermal cycles are obtained for different travel velocities.

3.3. Mechanical analysis

Fig. 5 shows contour plots of the *z*-component residual stress for layers 1, 3, 5, 7, and 9, after the part completely cools down to the room temperature, for different laser travel velocities. The plots look pixelated because an average value of the stress is calculated in each cell of the mesh; no smoothing has been applied. Large magnitudes of tensile stress are observed at the side surfaces and the edges of the plate. Compressive stresses dominate the inner region of the plate for all three cases. Similar residual stress contours are observed in all layers except in layer 9, which is close to the free end and hence is mostly stress-free. These observations agree with those reported by Rangaswamy et al. [12]. However, our results show a higher stress in the left edge of the plate compared with the right edge, while those of Ref. [12] look rather symmetric. We believe this is caused by the laser beam operation; in our experiments each layer was deposited from left to right, while in Ref. [12] the layers were deposited in both directions. Note also that the residual stress contours are similar for different laser travel velocities. This indicates that the laser travel velocity has no significant effect on the *z*-component of the residual stress distribution.

Figs. 6–10 show the profiles of the *y*- and *z*-components of residual stress at the center line of layers 1, 3, 5, 7, and 9, along the laser travel direction for different laser travel velocities. The scattered points are modeling results for each laser travel velocity and the solid lines are fitting curves to the modeling results. The dashed horizontal line in the *z*-stress profiles is the average value of the *z*-component residual stress for each layer. For the *z*-component residual stress, a similar trend was obtained for different laser travel velocities. Tensile stress at both ends of the plate and compressive stress inside the plate are observed. This is consistent with the experimental investigations in references [11,12].

For the *y*-component of the residual stress, similar trends are obtained for the laser travel velocities of 2.5 and 4.2 mm/s. These include near-zero stress at both ends of the plate and compressive stress inside the plate. However, a tensile stress is observed inside the plate for the laser travel velocity of 8.5 mm/s. We believe that this occurs because a high velocity of deposition gives less time to material stretched in the *y*-direction due to differential cooling rate to recover its position, resulting in a high tensile stress. We are not aware that this behavior at higher travel velocities, which is important in deciding process parameters, has been reported before.

Fig. 11 shows the distribution of the *y* and *z*-components of the residual stress along the vertical centerline from the plate-free end to the substrate, for different laser travel velocities. For the *z*-component residual stress (Fig. 11(a)), zero stress is obtained at the top-free end of the part and the stress decreases with the distance from the free end. Similar trends are obtained for all three-laser travel velocities. For the *y*-component residual stress (Fig. 11(b)), tensile stresses are obtained at a laser travel velocity of 8.5 mm/s and compressive stresses are presented for laser travel velocities of 2.5 and 4.2 mm/s.

Figs. 12–15 show a comparison of the residual stress profiles obtained by modeling and measurements. Figs. 12 and 13 show stress profiles for a laser travel speed of 4.2 mm/s. The solid line is
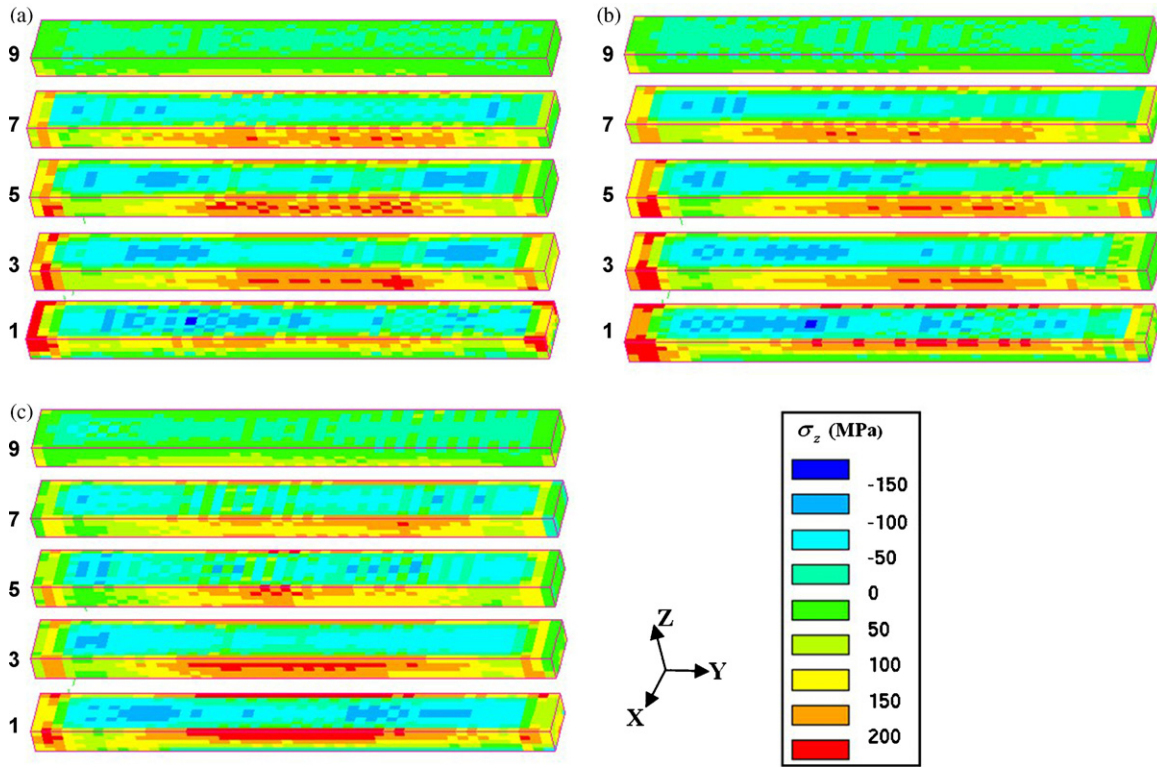
Fig. 5. Contours of the z-component residual stress for each layer after the part cools down to room temperature for travel velocity: (a) 2.5 mm/s; (b) 4.2 mm/s; (c) 8.5 mm/s.
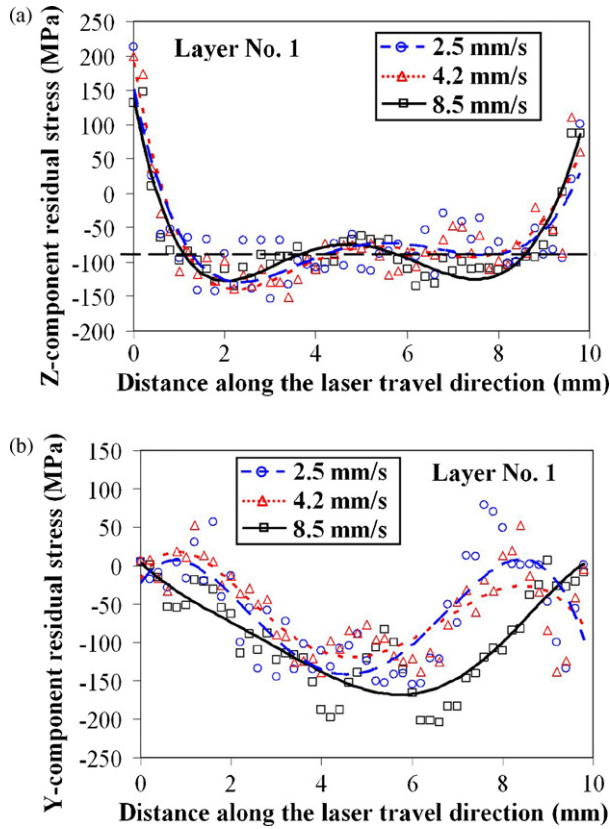

Fig. 6. Residual stresses along the laser travel direction at the surface of the 1st layer for different laser travel speeds (a) σ_z and (b) σ_y (scattered points are modeling results; solid lines are the fitting curves for each travel speed; horizontal line is average value).
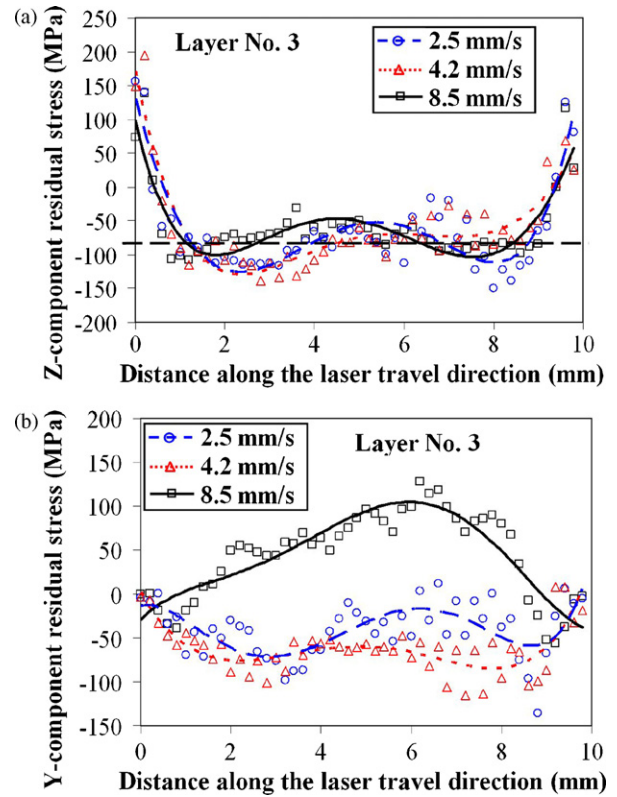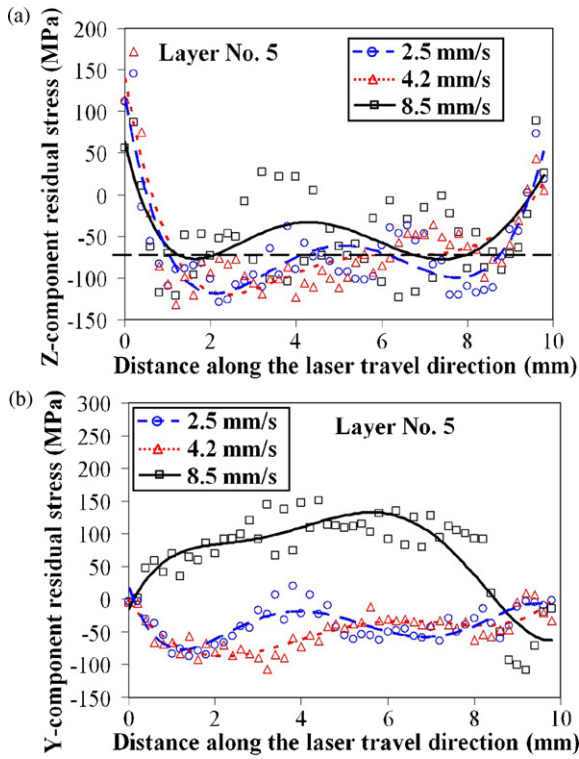
Fig. 7. Residual stresses along the laser travel direction at the surface of the 3rd layer for different laser travel speeds (a) σ_z and (b) σ_y (scattered points are modeling results and solid lines are the fitting curves for each travel speed; horizontal line is average value).
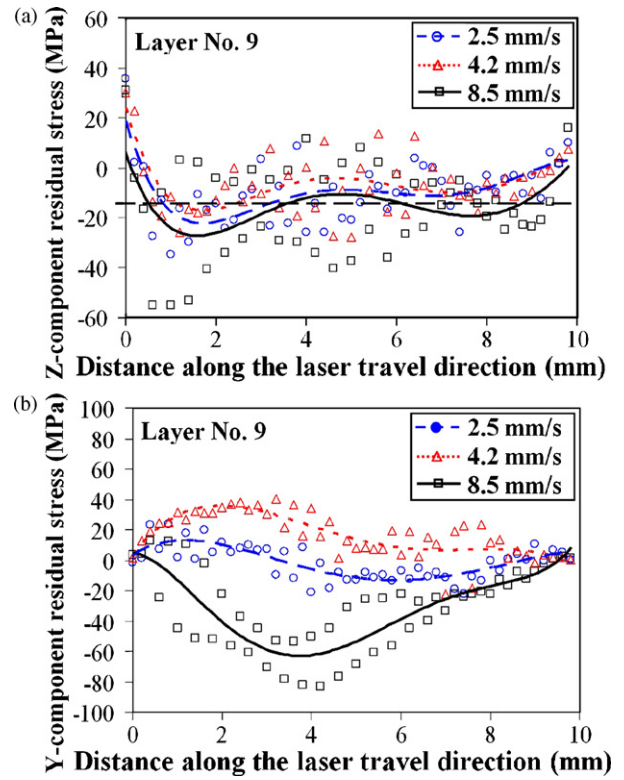
Fig. 8. Residual stresses along the laser travel direction at the surface of the 5th layer for different laser travel speeds (a) σ_z and (b) σ_y (scattered points are modeling results and solid lines are the fitting curves for each travel speed; horizontal line is average value).
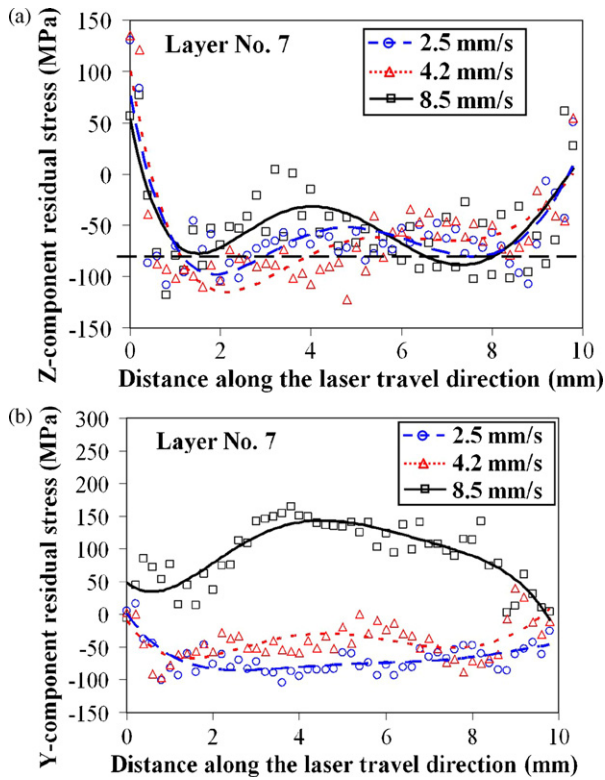

Fig. 9. Residual stresses along the laser travel direction at the surface of the 7th layer for different laser travel speeds (a) σ_z and (b) σ_y (scattered points are modeling results and solid lines are the fitting curves for each travel speed; horizontal line is average value).

Fig. 10. Residual stresses along the laser travel direction at the surface of the 9th layer for different laser travel speeds (a) σ_z and (b) σ_y (scattered points are modeling results and solid lines are the fitting curves for each travel speed; horizontal line is average value).
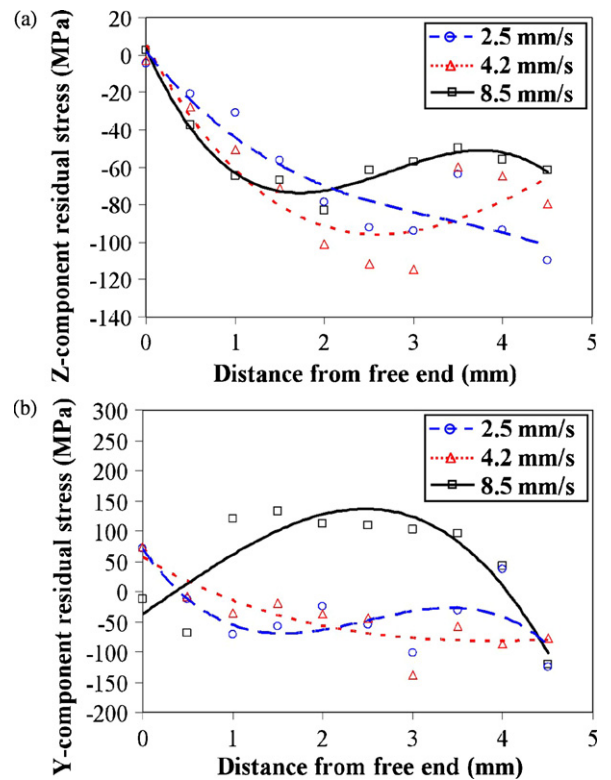

Fig. 11. Residual stresses along the centerline of vertical direction for different laser travel speeds (a) σ_z and (b) σ_y (scattered points are modeling results and solid lines are the fitting curves).
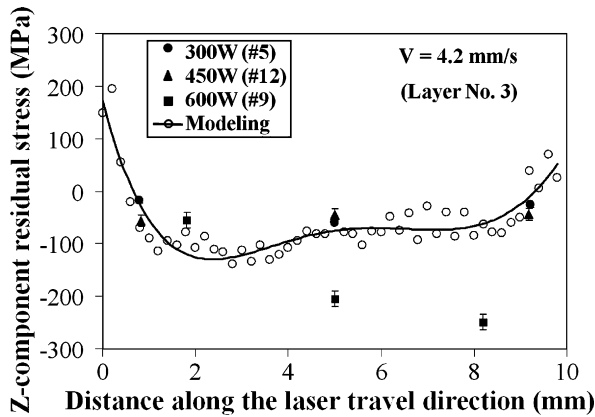
Fig. 12. Comparison between experimental data with different laser powers (300, 450, and 600 W) and calculated residual stress σ_z along the laser travel direction at the surface of the 3rd layer for $V = 4.2$ mm/s (Solid lines are the fitting curves of modeling results; error bars are shown in each experimental data).
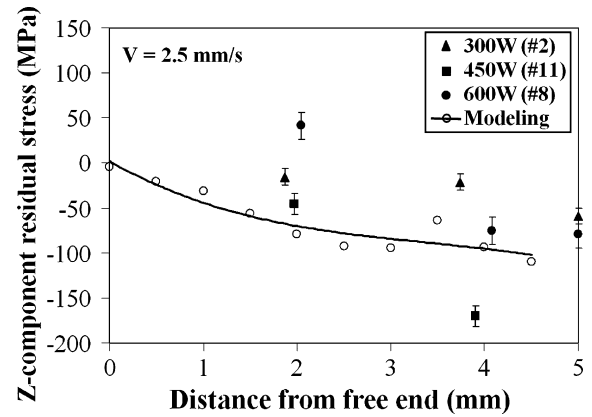

Fig. 13. Comparison between experimental data with different laser powers (300, 450, and 600 W) and calculated residual stress σ_z along the centerline of vertical direction for $V = 4.2$ mm/s (solid lines are the fitting curves of modeling results; error bars are shown in each experimental data).
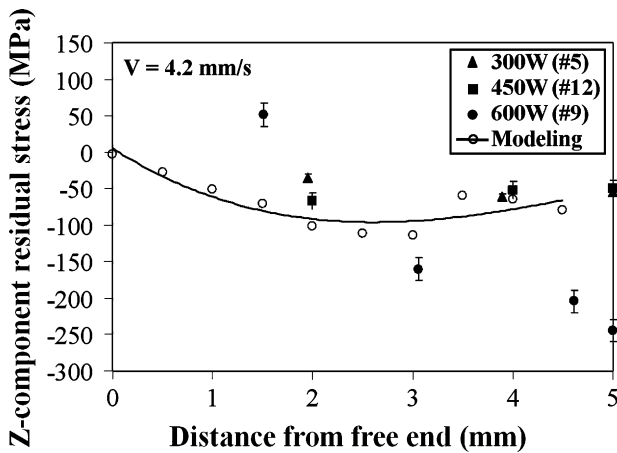

Fig. 14. Comparison between experimental data with different laser powers (300, 450, and 600 W) and calculated residual stress σ_z along the laser travel direction at the surface of the 3rd layer for $V = 2.5$ mm/s (solid lines are the fitting curves of modeling results; error bars are shown in each experimental data).

Fig. 15. Comparison between experimental data with different laser powers (300, 450, and 600 W) and calculated residual stress σ_z along the centerline of vertical direction for $V = 2.5$ mm/s (solid lines are the fitting curves of modeling results; error bars are shown in each experimental data).
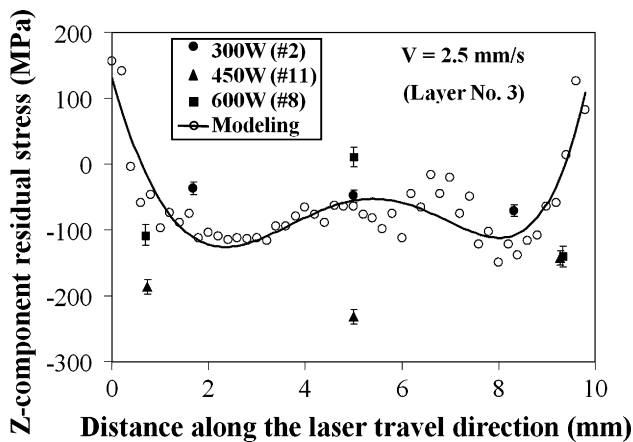
a fitting curve of simulated stress values (hollow circular points), while the solid points are measured residual stresses for different levels of the laser power. Because the real samples are taller and wider than the simulated model sample, the horizontal profile comparison is done for the first 5 mm measured from the vertical centerline, while the vertical profile comparison is done for the first 5 mm measured from the free end. This limits the comparison to 3 or 4 measured data points for each profile. It can be observed that the simulated profiles for both the horizontal direction (Fig. 12) and vertical direction (Fig. 13), agree rather well with the measured data corresponding to a laser power of 300 W, which is close to the average value of 285 W used in the simulations through the optimized laser power program.

This is a noticeable agreement, considering the several simplifications used in the construction of the model. In particular, it seems to indicate that the constitutive model utilized for the material performs satisfactorily in predicting the overall level of the σ_z residual stress. However, more experimental validations in a wider range of process parameters would be necessary to confirm this observation.

Figs. 14 and 15 show the model-experiment comparison for stress profiles under a laser travel speed of 2.5 mm/s. In this case, the simulated values align more closely with the experimental points corresponding to a laser power of 300 W, when looking at the horizontal stress profile (Fig. 14). However, in the vertical profile (Fig. 15), it is observed that the simulation predicts lower stress than the one indicated by the experimental points, because the average power used in the simulation for this laser speed was 254 W. This suggests a slight dependence of residual stress with laser power, producing higher stress for larger laser powers.

4. Conclusions

This study presented a finite element model to calculate the residual stress in AISI 410 stainless steel (SS410) LENS-deposited single wall plates. For the z-component residual stress, compressive stress inside the plate and tensile stress at both ends of the plate are obtained. The laser travel velocity has no significant effect on the z-component residual stress in the range of this study. Higher laser powers can increase the magnitude of the z-component residual stress. For the y-component residual stress, compressive residual stress is presented for laser travel velocities of 2.5 and 4.2 mm/s, however, tensile residual stress is obtained for a laser travel velocity of 8.5 mm/s. The main contribution of this study is to quantify the

effects of two of the most important LENS parameters, laser power and travel speed, on the residual stress level of built parts, using a finite element model and neutron diffraction stress measurements. The comparison between the experimental and modeling results shows a fairly good agreement, although further studies in a wider range of parameters would be necessary to validate the predicting capability of the model.

Acknowledgements

References

[1] C.L. Atwood, M.L. Griffith, M.E. Schlienger, L.D. Harwell, M.T. Ensz, D.M. Keicher, M.E. Schlienger, J.A. Romero, J.E. Smugeresky, Proceedings of ICALEO 98, Orlando, FL, November 16–19, 1998, pp. E-1–E-7.
[2] J. Mazumder, H. Qi, Proceedings of SPIE The International Society for Optical Engineering 5706, 2005, pp. 38–59.
[3] D.M. Keicher, W.D. Miller, J.E. Smugeresky, J.A. Romero, TMS Annual Meeting, Hard Coatings Based on Borides, Carbides & Nitrides: Synthesis Characterization & Application (1998) 369–377.
[4] J.A. Brooks, T.J. Headley, C.V. Robino, Mater. Res. Soc. Symp. Proc. 625 (2000) 21–30.
[5] J.A. Brooks, C.V. Robino, T.J. Headley, J.R. Michael, Weld. J. (Miami, FL) 82 (2003) 51/S–64/S.
[6] W. Liu, J.N. Dupont, Metal. Mater. Trans. A 34 (2003) 2633–2641.
[7] M.L. Griffith, M.T. Ensz, J.D. Puskar, C.V. Robino, J.A. Brooks, J.A. Philliber, J.E. Smugeresky, W.H. Hofmeister, Mater. Res. Soc. Symp. Proc. 625 (2000) 9–20.
[8] S.M. Kelly, S.L. Kampe, C.R. Crowe, Mater. Res. Soc. Symp. Proc. 625 (2000) 3–8.
[9] S.M. Kelly, S.L. Kampe, Metal. Mater. Trans. A 35 (2004) 1869–1879.
[10] F.J. Kahlen, A. Kar, J. Laser Appl. 13 (2001) 60–69.
[11] P. Rangaswamy, M.L. Griffth, M.B. Prime, T.M. Holden, R.B. Rogge, J.M. Edwards, R.J. Sebring, Mater. Sci. Eng. A 399 (2005) 72–83.
[12] P. Rangaswamy, T.M. Holde, R. Rogge, M.L. Griffith, J. Strain Anal. Eng. Des. 38 (2003) 519–527.
[13] M.L. Griffith, M.E. Schlienger, L.D. Harwell, M.S. Oliver, M.D. Baldwin, M.T. Ensz, J.E. Smugeresky, M. Essien, J. Brooks, C.V. Robino, W.H. Hofmeister, M.J. Wert, D.V. Nelson, J. Mater. Des. 20 (1999) 107–114.
[14] P.J. Maziasz, E.A. Payzant, M.E. Schlienger, K.M. McHugh, Scripta Mater. 39 (1998) 1471–1476.
[15] A. Vasinonta, J.L. Beuth, M.L. Griffith, J. Manuf. Sci. Eng. 129 (2007) 101–109.
[16] M. Labudovic, D. Hu, R. Kovacevic, J. Mater. Sci. 38 (2003) 35–49.
[17] A.H. Nickel, D.M. Barnett, F.B. Prinz, Mater. Sci. Eng. A 317 (2001) 59–64.
[18] SYSWELD 2005 Reference and Example Manuals, ESI Group, 2005.
[19] SYSWELD 2005 Analysis Reference Manual, ESI Group, 2005.
[20] S.A. Tsirkas, P. Papanikos, Th. Kermanidis, J. Mater. Process. Technol. 134 (2003) 59–69.
[21] L. Wang, S.D. Felicelli, J.E. Craig, P.T. Wang, M.F. Horstemeyer, Proceedings of The Eighteenth Solid Freeform Fabrication Symposium, Austin, TX, 2007, pp. 100–111.
[22] L. Wang, S.D. Felicelli, Mater. Sci. Eng. A 435/436 (2006) 625–631.
[23] L. Wang, S.D. Felicelli, Y. Gooroochurn, P.T. Wang, M.F. Horstemeyer, Mater. Sci. Eng. A 474 (2008) 148–156.
[24] L. Wang, S.D. Felicelli, J. Manuf. Sci. Eng. 129 (2007) 1028–1034.
[25] L. Wang, S.D. Felicelli, Y. Gooroochurn, P.T. Wang, M.F. Horstemeyer, Proceedings of The Seventeenth Solid Freeform Fabrication Symposium, Austin, TX, 2006, pp. 453–463.
[26] L. Wang, S.D. Felicelli, in: P. Anyalebechi (Ed.), Materials Processing Fundamentals, TMS (The Minerals, Metals & Materials Society), 2007, pp. 63–72, IBN: 978-0-87339-674-5.
[27] L. Wang, P. Pratt, S.D. Felicelli, C.R. Hubbard, TMS Annual Meeting & Exhibition, New Orleans, LA, March 9–13, 2008.